

# The X-Ray Photoionized Wind in Cen X-3/V779 Cen

Patrick S. Wojdowski, Duane A. Liedahl

*Physics Department, Lawrence Livermore National Laboratory*

*P.O. Box 808, Livermore, CA 94551*

patrickw@virgo.llnl.gov

duane@virgo.llnl.gov

and

Masao Sako

*Columbia Astrophysics Laboratory and Department of Physics, Columbia University, 538 West  
120th St., New York, NY 10027*

masao@astro.columbia.edu

## ABSTRACT

We analyze the *ASCA* spectrum of the Cen X-3 X-ray binary system in eclipse using atomic models appropriate to recombination-dominated level population kinetics in an overionized plasma. In order to estimate the wind characteristics, we first fit the eclipse spectrum to a single-zone photoionized plasma model. We then fit spectra from a range of orbital phases using global models of photoionized winds from the companion star and the accretion disk that account for the continuous distribution of density and ionization state. We find that the spectrum can be reproduced by a density distribution of the form derived by Castor, Abbott, & Klein (1975) for radiation-driven winds with  $\dot{M}/v_\infty$  consistent with values for isolated stars of the same stellar type. This is surprising because the neutron star is very luminous ( $\sim 10^{38}$  erg s $^{-1}$ ) and the X-rays from the neutron star should ionize the wind and destroy the ions that provide the opacity for the radiation-driven wind. Using the same functional form for the density profile, we also fit the spectrum to a spherically symmetric wind centered on the neutron star, a configuration chosen to represent a disk wind. We argue that the relatively modest orbital variation of the discrete spectrum rules out a disk wind hypothesis.

## 1. Introduction

Since the early observations of the High Mass X-ray Binary (HMXB) Cen X-3, it has been known that the system exhibits a residual X-ray flux in eclipse, indicating that the X-rays are

scattered or otherwise reprocessed, as might occur in a wind (Schreier et al. 1972). A similar phenomenon has been observed in other HMXBs — for example, Becker et al. (1978) observed a residual eclipse flux from Vela X-1. It has been realized since the far ultraviolet became accessible with rocket and satellite-borne instruments that isolated hot stars expel material at rates of order  $10^{-6} M_{\odot} \text{ yr}^{-1}$  (Morton 1967), and so the existence of winds in HMXBs might have been expected. It was shown that in isolated hot stars, strong winds are driven by transfer of the outward momentum of the ultraviolet stellar radiation to the matter through line absorption (Lucy & Solomon 1970; Castor et al. 1975).

However, it was pointed out by Hatchett & McCray (1977) that in an X-ray binary, X-rays from the compact object would ionize a part of the wind around the X-ray source to such a high degree that the ions with line transitions which enable radiative driving would not be present. Presumably, if an X-ray source were luminous enough, it could completely shut off the radiation driven wind on the X-ray illuminated side of the companion star. Calculations by MacGregor & Vitello (1982) showed that radiative driving is disabled for X-ray luminosities larger than  $\sim 5 \times 10^{34} \text{ erg s}^{-1}$ . As HMXBs typically have luminosities in the range  $10^{36}$ – $10^{38} \text{ erg s}^{-1}$ , this would indicate that radiative driving could not function at all in X-ray binaries. However, this calculation assumed that the wind is optically thin to the ionizing X-rays. The effects of the wind’s opacity to X-rays has been explored by Masai (1984) and by Stevens (1991). These calculations considered the formation of a  $\text{He}^{++}/\text{He}^{+}$  Strömgren surface in the wind. On the  $\text{He}^{+}$  side of this boundary, all elements have lower ionization, and more of the ions necessary for radiative driving are present. Masai (1984) concluded that most wind-fed X-ray binaries must contain Strömgren boundaries and hence radiative winds. This conclusion is limited to wind-fed systems because of the coupling of the wind parameters to the accretion luminosity in these systems. An increase in the luminosity of the X-ray source tends to increase the volume of the  $\text{He}^{++}$  region, however, to increase the luminosity it is necessary to increase the mass loss rate of the companion star or decrease the wind velocity, both of which tend to decrease the volume of the  $\text{He}^{++}$  region. The investigation of Stevens (1991) was not limited to wind-fed systems. It showed that X-ray luminosities as large as  $\sim 10^{36} \text{ erg s}^{-1}$  diminished the wind velocity and mass loss rate but did not completely shut off the wind. However, for luminosities larger than  $4 \times 10^{36} \text{ erg s}^{-1}$  Stevens (1991) was “unable to find dynamical solutions” for the wind. Ho & Arons (1987) explored the behavior of high luminosity (exclusively) wind-fed X-ray binaries. However, they did not explicitly consider optical depth effects and their condition for X-ray ionization turning off the wind is questionable, even for the optically thin case (c.f. Stevens 1991). We regard the nature of winds in X-ray binaries outside of the X-ray shadow of the companion as unresolved, and especially problematic in the case of high luminosity ( $L_X \sim 10^{38} \text{ erg s}^{-1}$ ) systems.

A wind driving mechanism which does not depend on the presence of ions with UV resonance lines is thermal pressure due to X-ray heating of the exposed face of the companion star (also referred to as evaporative winds). This mechanism was invoked by Basko & Sunyaev (1973) and by Arons (1973) to explain the mass transfer in Her X-1, though Alme & Wilson (1974) and McCray

& Hatchett (1975) found that a thermal wind alone could not power the X-ray source. Day & Stevens (1993) showed that an X-ray excited wind could account for the mass transfer in Cen X-3, as well as explain the extended eclipse transitions seen in the source. At least one simulation of the disk-fed high-mass X-ray binary LMC X-4, in which the effects of X-ray heating were included, showed that a stronger wind was driven from the accretion disk, and that the structure of the wind was dominated by the disk wind (Owen & Blondin 1997).

Before the launch of *ASCA* in 1993 the energy resolution of most cosmic X-ray detectors was rather poor ( $\Delta E/E \sim 10\text{--}20\%$ ) and therefore, these instruments were unable to detect the X-ray emission lines which are a signature of optically thin, highly ionized gas. Nor is there any other waveband in which discrete emission from very highly ionized gas could be detected. Most observational X-ray examinations of winds in HMXBs focused on absorption in low-ionization material, iron fluorescence, which is produced primarily in low-ionization material, and the Compton scattering continuum which is insensitive to the ionization state. (Kallman & White 1982; Nagase et al. 1986; Sato et al. 1986; Clark et al. 1988; Haberl et al. 1989; Woo et al. 1995). The lack of a regular low-ionization wind on the X-ray illuminated side of HMXBs, and therefore the presence of a high-ionization wind there, has been inferred from decreases in equivalent widths and velocities of the P Cygni profiles of ultraviolet resonance lines away from X-ray eclipse (Dupree et al. 1980; van der Klis et al. 1982; Hammerschlag-Hensberge et al. 1984; Vrtillek et al. 1997). However, direct study of the highly ionized material requires X-ray spectroscopy. The Solid-state Imaging Spectrometers (SIS, Gendreau 1995) on board *ASCA* have energy resolution of a few per cent which allows identification and study of many previously undetectable X-ray spectral features. With the SIS detectors, recombination and fluorescence emission features were seen from several ions from the HMXBs Vela X-1 (Nagase et al. 1994), Cen X-3 (Ebisawa et al. 1996), and Cyg X-3 (Kitamoto et al. 1994; Liedahl & Paerels 1996; Kawashima & Kitamoto 1996).

When a compact X-ray source is occulted by its companion, the emission spectrum from an extended wind can be studied without the confusion from the more intense, generally featureless, spectrum of X-rays from the neutron star. Sako et al. (1999) studied the eclipse spectrum of the low luminosity HMXB Vela X-1 obtained by *ASCA* and estimated the rate of mass loss. Though a highly ionized wind exists in Vela X-1, they found that most of the mass is inside dense clumps, which are not highly ionized. This allows for the possibility that radiation imparts its outward momentum to the clumps which then drag the hot, diffuse wind outward. Presumably, these clumps could be destroyed (or inhibited from forming) by a more luminous X-ray source such as Cen X-3 or SMC X-1. In fact, Ebisawa et al. (1996) showed that the equivalent width of the 6.4 keV iron fluorescence line in Cen X-3 was nearly constant with orbital phase, indicating that most of the low-ionization material in the system is located near the neutron star, and that very little low-ionization material is found in the extended wind. This is also confirmed by pulsations in the 6.4 keV line (Day et al. 1993; Audley 1998). Wojdowski, Clark, & Kallman (2000) used hydrodynamic simulations of the wind in the most luminous persistent HMXB SMC X-1 by Blondin & Woo (1995) to predict the X-ray eclipse spectrum of that system and compared it to a spectrum obtained with *ASCA*. In the

simulation, a tenuous, very highly ionized wind formed on the X-ray illuminated side and a denser wind developed on the X-ray shadowed side. However, dense finger-like structures protruding from the shadowed side of the companion were swept into the X-ray illuminated region by the Coriolis force. The calculations showed that the reprocessed radiation from the tenuous gas was dominated by Compton scattering and the denser gas emitted copious amounts of recombination radiation. The observed spectrum was nearly featureless however, and Wojdowski et al. (2000) concluded that the dense fingers that appeared in the simulation could not be present in the wind of SMC X-1.

Cen X-3 is one the most luminous, persistent known HMXBs in the Galaxy. It consists of a 4.8 second pulsar in a 2.08 day eclipsing orbit (Schreier et al. 1972) with its O6–8 III type (Conti 1978; Hutchings et al. 1979) companion V779 Cen. The high X-ray luminosity of Cen X-3 makes it an excellent candidate for the study of X-ray photoionized winds. It was observed by *ASCA* over approximately half an orbit, which included an eclipse. Ebisawa et al. (1996) found several emission lines in this data set, which were mostly from hydrogen-like ions. From the intensities of these lines, they made estimates of the scale and physical conditions of the wind.

We re-analyze the data set of Ebisawa et al. (1996) using the observed spectra to test physically motivated wind models with the goal of providing constraints on the wind driving mechanism. In § 2 we describe our reduction of the data. In § 3, we calculate emission spectra for photoionized plasmas using a list of  $\sim 3000$  lines and emission features, fit the observed spectra using single zone emission spectra and then use the results to estimate wind parameters. In § 4 we calculate spectra using explicit parameterized models of the wind density distribution, and fit the observed spectra to determine wind parameters more accurately. We test two explicit global wind models: 1) a stellar wind from the companion with the velocity profile of a radiatively driven wind and 2) motivated by the accretion disk wind in the simulation of Owen & Blondin (1997), a wind with the same velocity profile but centered on the neutron star. In § 5 we justify an assumption that the wind is optically thin to X-rays which is used in previous sections. In § 6, we discuss the implications of our results.

## 2. Data Reduction

We obtained the screened REV2 *ASCA* event data from the 1993 June 24-25 observation of Cen X-3 across an eclipse from the HEASARC archive. All manipulation of the data was done with FTOOLS v4.2 (The Ftools Group 1998) and all of the programs mentioned in this section are from that package. We divided the data into the same four time segments as Ebisawa et al. (1996), corresponding to phase ranges  $-0.31$  to  $-0.29$ ,  $-0.23$  to  $-0.08$ ,  $-0.08$  to  $0.13$ , and  $0.14$  to  $0.20$ . The data was taken in a mix of FAINT and BRIGHT modes. For the data taken in FAINT mode, we used the files which had been converted to BRIGHT mode on the ground in order to have homogeneous data. For each of the time segments, we extracted all counts from inside a circle of radius  $191''$ . We extracted a background spectrum from an annulus of inner radius  $191''$  and outer radius  $382''$ . During the observation, the center of the image was placed so that the source counts were distributed over all four of the detector chips. During the eclipse phase, all four chips

were on but during the rest of the observation only one of the four chips was on, resulting in a  $\sim 45\%$  collection efficiency due to the placement of the source near the chip boundary. The spectra were extracted with the standard channel binning applied by XSELECT resulting in 512 energy channels. The spectra from the different chips of each detector and from the two SIS detectors from the same time interval were added using ADDASCASPEC. The energy channels in the range 2.9–8.0 keV were binned additionally by a factor of two. Additional binning was applied to the energy channels in the range 8.0–10.0 keV so that each channel in the eclipse spectrum had at least 50 counts.

The analysis tools we used to compute the detector response include the reduction in effective area due to the fact the source areas we have chosen do not include all of the photons focussed by the mirrors. However, the background regions also contain some source photons which are subtracted from the source spectrum in computing the background selection region. Our source region (for all chips on) contains approximately 80% of the photons for a point source at the center and our background region contains approximately 15% (Serlemitsos et al. 1995). The background spectrum is multiplied by the area of the source region and divided by the area of the background region and then subtracted from the source spectrum. Because the background region is larger than the source region by a factor of 3, approximately 5% of the source flux is subtracted from the source spectrum. This effect is not accounted for by our analysis. This problem is compounded by the fact that the image of Cen X-3 is further smeared, in a way which depends on energy, due to an X-ray halo and this halo is delayed in time relative to the direct photons. However, the radius of the halo is approximately the size of the source region and the surface brightness due to the halo is generally no larger than that due to the image of the direct photons (Woo et al. 1994) and therefore leads to a similar subtraction of source photons. Because of the complexity of these effects, we do not try to account for them explicitly but note that fluxes (and quantities proportional to flux) which we derive are too small by approximately a factor 10%. This error does not qualitatively affect any of the results we derive in this work.

### 3. Single-Zone Spectral Models

Emission spectra from X-ray binaries are generally interpreted with the assumption that photoionization from the compact X-ray source is the dominant source of ionization in the circumstellar plasma. This is justified by the relative values of the luminosities of the X-ray sources and the densities and linear scales of the system. While it is straightforward to measure X-ray luminosities and, where orbital parameters are available from pulsar timing and optical spectroscopy, linear scales in X-ray binaries, determinations of the matter density that do not depend on the assumption of photoionization equilibrium are less reliable. Photoionization equilibrium has been inferred directly from observed X-ray recombination spectra (e.g., Liedahl & Paerels 1996). In the case of Cen X-3 however, there are no obvious spectral signatures of recombination dominance. The observed spectrum consists mainly of  $\text{Ly}\alpha$  transitions from hydrogen-like ions which, in principle, can

be produced in plasmas where collisions dominate the ionization. We therefore attempt to fit the eclipse spectrum of Cen X-3 with spectral models of emission from collisionally ionized (coronal) plasma as well as photoionized plasmas.

The X-ray spectrum observed from Cen X-3 includes at least the following components: direct emission from the neutron star, X-rays from the neutron star which have been scattered in the wind, continuum and line emission from the wind and other circumstellar material, and X-rays scattered from interstellar dust grains. All of these components contribute to the observed continuum, but only the wind and circumstellar material can emit lines. We found that, in general, it was possible to fit the continuum using two power laws, each absorbed by a different column density. The more highly absorbed power-law may correspond approximately to the X-rays from the neutron star viewed through some dense component of circumstellar material and the less absorbed power-law to the neutron star continuum scattered in the extended wind and by dust. However, since our primary goal is to extract and interpret the emission line spectrum, we do not attempt to constrain the parameters of these power laws in a manner that would force them to correspond to physical sources of continuum emission (c.f., Ebisawa et al. 1996). We interpret the lines, except for the 6.4 keV Fe  $K\alpha$  line as emission from the extended wind. These plasma emission models are described in detail below. The spectral model is,

$$\mathcal{F}(\epsilon) = e^{-\sigma(\epsilon)N_{H1}} \left\{ f_{pl1}(\epsilon) + f_{plasma}(\epsilon) + e^{-\sigma(\epsilon)N_{H2}} [I_{line}\delta(\epsilon - \epsilon_{line}) + f_{pl2}(\epsilon)] \right\} \quad (1)$$

where the power laws,

$$f_{pli}(\epsilon) = K_{pli} \left( \frac{\epsilon}{1 \text{ keV}} \right)^{-\alpha_i}, \quad (2)$$

$f_{plasma}$  is the plasma emission model,  $\sigma(\epsilon)$  is the interstellar absorption cross-section of Morrison & McCammon (1983),  $N_{Hi}$  are the absorption column densities,  $I_{line}$  is the line photon flux and  $\delta$  is the Dirac delta function, used for the the 6.4 keV Fe  $K\alpha$  line complex. The energy of the Fe  $K\alpha$  line,  $\epsilon_{line}$ , was constrained to be in the range 6.3–6.5 keV. The Fe  $K\alpha$  line was the only fluorescent feature required to fit the data in any of our fits. Ebisawa et al. (1996) identified an emission feature at energy  $1.25 \pm 0.04$  keV with the 1.25 keV Mg I  $K\alpha$  fluorescent line. However, in all of our spectral models described here, this emission feature is fully accounted for by Ne X  $Ly\beta$  (1.21 keV).

When the neutron star is eclipsed by the companion star, the X-rays from the extended wind only are observed. Therefore, for the purpose of testing basic plasma emission models, we fit only the spectrum from eclipse. For our spectral fits, we used the XSPEC spectral fitting program (v10.0, Arnaud 1996), importing our own models for emission from photoionized plasmas.

### 3.1. Collisional Ionization Equilibrium

We fit the eclipse spectrum, using for  $f_{plasma}$  the emission spectrum of an isothermal plasma in collisional ionization equilibrium (CIE). Also referred to as coronal equilibrium, this describes a situation where recombination is balanced by collisional ionization by electrons, and ionization

by radiation is negligible. We use the MEKAL model (Mewe et al. 1996) contained in XSPEC for the CIE plasma emission. The three parameters of the MEKAL model are the temperature, metal abundance, and the normalization. The emission processes in CIE are determined by two-body interaction rates, so the normalization of the flux is proportional to the emission measure ( $E \equiv \int n_e^2 dV$ ) divided by the square of the distance to the source. The best fit parameters are shown in Table 1, and the spectrum is plotted in Figure 1.

The MEKAL model, with best-fit parameters, which reproduces most of the the observed emission lines, also accounts for all of the continuum emission below  $\sim 4$  keV through bremsstrahlung radiation from the same gas. For parameters for which the MEKAL model accounts for the observed line emission, the model also accounts for all of the continuum emission below  $\sim 4$  keV. However, collisionally ionized gas must also scatter X-rays from the neutron star. In the *ASCA* band, optically thin electron scattering reproduces the continuum shape of the X-ray source with a fractional luminosity relative to the source spectrum equal to:

$$\frac{L_{\text{scat}}}{L} = \frac{\sigma_{\text{T}}}{4\pi} \int \frac{n_e}{r^2} dV, \quad (3)$$

where  $\sigma_{\text{T}}$  is the Thomson cross-section and  $r$  is the distance from the compact source. We can estimate this fraction by taking the orbital separation  $a$  as the linear scale of the system and setting:

$$r = a, \quad n_e = (E/V)^{1/2}, \quad V = \frac{4\pi}{3} a^3. \quad (4)$$

Then,

$$\frac{L_{\text{scat}}}{L} \approx (12\pi)^{-1/2} \sigma_{\text{T}} E^{1/2} a^{-1/2} = 1.6 \times 10^{-2} \quad (5)$$

If the neutron star has an intrinsic spectrum in the 2–10 keV band which is a power law with photon index 1.5, and luminosity  $\sim 10^{38}$  erg s $^{-1}$ , then, using the system parameters of Table 2, the Compton scattered luminosity in the 2–10 keV band should be  $\sim 10^{36}$  erg s $^{-1}$ . This corresponds to a power-law normalization of  $I_{\text{pl}} = 1.6 \times 10^{-2}$  s $^{-1}$  cm $^{-2}$  keV $^{-1}$ . However, the upper limit on  $I_{\text{pl}}$  from the fit,  $1.1 \times 10^{-4}$  s $^{-1}$  cm $^{-2}$  keV $^{-1}$ , corresponds to a scattered luminosity of  $7 \times 10^{33}$  erg s $^{-1}$ . In principle, it is possible that the Compton scattered continuum could be reduced relative to the thermal emission due to clumping of the wind. If the wind is clumped with volume filling factor  $f$ , then the density would have to be increased by a factor  $f^{-1/2}$  to preserve the emission measure. The new Compton scattered flux would then be changed by a factor  $f^{1/2}$  since its magnitude is proportional to  $nV$ . A very small filling factor ( $f \approx 10^{-4}$ ) would be necessary however and we regard this as unlikely. We therefore reject this model.

Increasing the metal abundance in the gas increases the flux of the lines relative to the bremsstrahlung continuum, thereby providing “room” for a scattered continuum component. Therefore, we tried another fit in which we allowed the metal abundance to be free. For this fit, we tied the normalization of the first power law (pl1) to the emission measure of the MEKAL component as described above (Eq. 5). XSPEC does not allow the user to set one parameter to the square root of another parameter, so we fixed the power-law normalization according to a trial value of the

emission measure, fit, and iterated to find a best fit emission measure with a consistent power-law normalization. This procedure resulted in a statistically acceptable fit (Table 1, Figure 2). The lower limit on the abundance derived from this procedure, however, is 25 times solar, which we believe to be implausibly high. and so we reject this model as well.

### 3.2. Photoionization Equilibrium

Having rejected plausible collisional ionization spectral models, we proceed to fit the observed spectra using model emission spectra from photoionized plasmas. The radiation spectrum due to recombination consists of radiative recombination continua (RRC) from free electrons recombining directly to bound states and lines which are produced through radiative cascades. The volume emissivity of the recombination feature  $k$  is  $j_k = n_e n_{i+1} \alpha_k(T)$  where  $n_{i+1}$  is the density of the recombining ion to which the electron recombines. The function  $\alpha_k(T)$  is an effective recombination rate coefficient (the recombination coefficient for recombinations that produce transition  $k$ ) that depends on atomic parameters and the level population kinetics. In a gas which is optically thin and has density low enough such that all ions may be assumed to be in the ground state (i.e., the density is low compared to the critical density for all important transitions), the ion fractions and temperature are, for a given spectrum of ionizing radiation, functions only of the ionization parameter ( $\xi = L/nr^2$ , Tarter, Tucker, & Salpeter 1969). Therefore, for a photoionized plasma, the emissivity of any feature may be written  $j_k = n_e^2 f_k(\xi)$ , and, for the entire spectrum,  $j_\nu/n_e^2$  is a function only of  $\xi$ .

To calculate the temperature and ion fractions as a function of  $\xi$ , we need to know the X-ray spectrum of the neutron star. The best way to do this is to observe the X-ray spectrum from the neutron star directly while outside of eclipse. This *ASCA* data set includes data outside of eclipse. However, the observed spectra in these phases outside of eclipse differs greatly from the intrinsic spectrum of the neutron star because at the time of the observation the line of sight to the neutron star contained circumstellar material that substantially absorbed the direct X-rays. When circumstellar material passes in front of the neutron star, the direct X-rays are absorbed preferentially at low energies. Even when direct low energy X-rays are absorbed completely, low energy X-rays are still observed from scattering and emission from the extended wind, just as during eclipse by the companion star. The residual X-rays from scattering are generally not pulsed. The X-rays from Cen X-3 in this data set show both a spectrum which is deficient in low-energy X-rays compared to other observations (Nagase et al. 1992; Santangelo et al. 1998) and also are not pulsed at low energy (Ebisawa et al. 1996). Nagase et al. (1992) used similar evidence to demonstrate that a “pre-eclipse dip” observed by *Ginga* was due to absorption. In these out-of-eclipse intervals, the large absorption of the direct X-rays makes the strength of the direct flux comparable to and difficult to distinguish from the residual flux from scattering and wind emission, and it is impossible to isolate the flux from the neutron star in the observed spectrum. For the intrinsic spectrum of the neutron star, we instead use a spectrum obtained by Santangelo et al. (1998) with *BeppoSAX*.



Burderi et al. (2000) have shown that in this observation, the X-ray flux is pulsed down to the energy band below 1.8 keV indicating that it originates in the proximity of the neutron star. There is an additional advantage to using *BeppoSAX* in that it can measure the spectrum up to  $\sim 200$  keV. For  $\xi \gtrsim 10^4$ , the ions are nearly fully stripped, and the temperature is determined by Comptonization. The Compton temperature is highly sensitive to the presence of high energy photons. We used the “Lorenzian” model of Santangelo et al. (1998), extending the power-law continuum to low energy by setting the absorption column to zero, and excluding the cyclotron absorption feature, since a value for the depth of this feature is not provided.

We used the XSTAR program (v1.43, Kallman & Krolik 1999) to compute ion fractions and temperatures for 100 uniformly spaced values of  $\log \xi$  from  $-2$  to  $6$  using the Santangelo et al. (1998) spectrum. In the XSTAR calculation, we used a luminosity of  $10^{30} \text{ erg s}^{-1}$  and a constant density  $10^{-2} \text{ cm}^{-3}$  — again, for an optically thin gas, the absolute values of the luminosity and the density are not important. We then calculated the recombination spectrum at each value of  $\xi$  using the ion fractions and temperatures from XSTAR, and line and RRC powers calculated using the Hebrew University/Lawrence Livermore Atomic Code (HULLAC, Klapisch et al. 1977) and the Photoionization Cross-Section code (PIC, Saloman, Hubble, & Scofield 1988) for recombination cross-sections. These atomic models have been used to analyze the recombination spectrum of Cyg X-3 (Liedahl & Paerels 1996) and Vela X-1 (Sako et al. 1999) and are described further there.

We fit the eclipse spectrum using for  $f_{\text{plasma}}$  our recombination model spectra plus a corresponding bremsstrahlung component. The bremsstrahlung component is the BREMSS model from XSPEC. We tied the normalization of the bremsstrahlung component to that of the recombination component such that the emission measures would be equal. We set the temperature of the bremsstrahlung model to be a locally linear approximation to the function  $T(\log \xi)$  computed with XSTAR in the neighborhood of the best fit value of  $\log \xi$ . The best fit spectrum is shown in Figure 3, and the best fit parameters are shown in Table 1. The best fit value of the ionization parameter ( $\log \xi = 3.19$ ) corresponds to an electron temperature of 0.41 keV. At this temperature, the radiative recombination continua are broad, and so it is not surprising that they do not appear prominently in the spectrum. It is because of this that Ebisawa et al. (1996) were able to fit the spectrum using only lines and not RRC. This demonstrates that though the presence of prominent narrow RRC in emission spectra indicates photoionization (Liedahl & Paerels 1996), the lack of narrow RRC does not necessarily indicate some other type of equilibrium. It can be seen that the bremsstrahlung component is relatively faint, thus allowing a power-law continuum at low energies. The luminosity implied for the power-law component #1 is  $4 \times 10^{35} \text{ erg s}^{-1}$  which is much closer to the expected Compton scattered luminosity of  $\sim 10^{36} \text{ erg s}^{-1}$ . A quasi-continuum of blended lines and RRC accounts for 21% of the photon flux in the 1–3 keV band. This differs significantly from the individual line fits of Ebisawa et al. (1996) in which the lines constitute only 5% of the flux in this band.

From this single-zone fit, it is possible to make a crude estimate of the X-ray luminosity and parameters of the wind in Cen X-3, if we take the orbital separation to be the characteristic linear

scale of the system, and use our best fit value of the emission measure as in Equation 4. We then find for a characteristic wind density  $n \sim 5 \times 10^{10} \text{ cm}^{-3} (d/10 \text{ kpc})^{-1}$ . From the definition of  $\xi$ , we then have

$$L = \xi n r^2 \sim 1.4 \times 10^{38} \text{ erg s}^{-1} (d/10 \text{ kpc})^{-1}. \quad (6)$$

Note that this value of the luminosity is derived only from the flux of the recombination spectral features and the known system dimensions, yet it comes very close to the luminosity derived for Cen X-3 by measuring the continuum directly during the high state (Nagase et al. 1992; Santangelo et al. 1998). Ebisawa et al. (1996) derived similar, though somewhat larger, estimates for the characteristic density and luminosity ( $1.6 \times 10^{11} \text{ cm}^{-3}$  and  $1.8 \times 10^{38} \text{ erg s}^{-1}$  for  $d=10 \text{ kpc}$ ) using an emission measure derived from the fluxes of the 6.7 keV and 6.9 keV lines of, respectively, helium-like and hydrogen-like iron in the eclipse and egress spectra and by assuming a value of  $\log \xi = 3.4$  from their ratio. Our values differ because we use slightly different values for the linear scale and also because our values of  $\xi$  and  $E$  are derived from fitting all of the lines and not just the hydrogen- and helium-like iron lines.

We now estimate the characteristics of the stellar wind from this derived value of the density. In a spherically symmetric steady-state wind, continuity demands that:

$$\frac{\dot{M}}{v(R)} = 4\pi R^2 \mu n(R) \quad (7)$$

where  $\dot{M}$  is the mass-loss rate,  $v$  is the velocity,  $R$  is the distance from the center of the star,  $n$  is density of hydrogen (neutral and ionized), and the quantity  $\mu$  is the gas mass per hydrogen atom which we take to be  $1.4m_{\text{H}}$ . Again using the fiducial dimensions,  $\dot{M}/v \sim 4 \times 10^{-9} M_{\odot} \text{ yr}^{-1} (\text{km s}^{-1})^{-1} (d/10 \text{ kpc})^{-1}$  which, as will be discussed in § 6 below, is near values for isolated stars with spectral type similar to V779 Cen. While this model provides a statistically acceptable fit to the data, it is unlikely that the entire emission line region can be characterized by a single value of  $\xi$ . Therefore, we suggest that this model provides no more than a semi-quantitative description of the data. In the next section we use explicit wind models and spectra of all of the full phases of the observation to derive these wind parameters more accurately and to explore the wind geometry.

#### 4. Global Photoionized Wind Models

We use the recombination spectra described in the previous section to derive spectra for explicit wind density distributions. In order to calculate the global recombination spectrum of photoionized gas, we use the differential emission measure formalism (DEM, Sako et al. 1999). For an arbitrary distribution of gas, the total spectrum of recombination radiation is given by

$$L_{\nu} = \int \frac{j_{\nu}(\xi)}{n_e^2} \left[ \frac{dE}{d \log \xi} \right] d \log \xi, \quad (8)$$

where the quantity in brackets is the DEM distribution, which hereafter will be referred to as  $D(\xi)$ . In practice, we integrate only the volume of gas that is visible to the observer and refer to this as the apparent DEM. To calculate the DEM distribution, it is necessary to know only the density distribution of the gas and the luminosity of the radiation source. To calculate  $j_\nu(\xi)/n_e^2$ , it is necessary to know only the spectral shape of the ionizing radiation and the elemental composition of the gas. In this work, we calculate the spectrum of recombination emission from the wind of Cen X-3 for different models of the wind using different luminosities for the neutron star, but always using the same spectral shape for the neutron star X-ray emission and always assuming solar abundances (Anders & Grevesse 1989). The DEM formalism requires us to evaluate  $j_\nu(\xi)/n_e^2$  only once for a number of values  $\xi$ , and then, for different matter distributions and luminosities, to calculate the DEM distribution and evaluate the integral in Equation 8.

To calculate the DEM distribution for a given density distribution and luminosity, we divide the binary system into spatial cells. We then calculate  $\xi$  and the emission measure for each spatial cell. The emission measure for each cell is then added to a running sum of the emission measure for a  $\xi$  bin. Dividing the emission measure in each bin by the width of that bin in  $\log \xi$  gives the differential emission measure. If the density distribution is described by parameters such that the density everywhere scales linearly with one parameter, which we will call  $\eta$ , then to calculate the DEM distribution for new values of  $\eta$  and the luminosity  $L$  it is not necessary to recalculate the DEM distribution by summation over the spatial cells. For new values  $L'$  and  $\eta'$ , the new DEM distribution  $D'$  is related to the old DEM distribution  $D$  by

$$D' \left( \frac{L'\eta}{L\eta'} \xi \right) = \left( \frac{\eta'}{\eta} \right)^2 D(\xi). \quad (9)$$

This identity is derived in Appendix A. For a change in the luminosity and density parameter such that  $L'/\eta' = L/\eta$ , the DEM distribution is changed only by a constant factor  $(\eta'/\eta)^2 = (L'/L)^2$  and therefore so is the total emission spectrum.

#### 4.1. DEM Distributions for Model Winds

As alluded to in § 1, the structure of stellar winds in X-ray binaries are likely to be rather complicated. In addition to the effects of X-ray photoionization on the radiation driving, the gravity of the compact object and orbital motion may have a significant effect on the wind density distribution (e.g., Friend & Castor 1982). Though numerical simulations may account for many of these effects, we choose instead to use a simple, spherically symmetric density distribution with free parameters such that the density is easily recalculated for a change in parameters. We approximated the geometry of the X-ray binary system as a spherical star in orbit with a point-like neutron star emitting X-rays isotropically. For the dimensions of the system, we assumed the values in Table 2. We used density distributions for spherically symmetric, radiation driven winds (Castor et al. 1975; Kudritzki et al. 1989) from the companion star.

Modeling accretion disk winds introduces a new set of complications. They may be driven thermally (e.g., Woods et al. 1996), radiatively (e.g., Proga, Stone, & Drew 1999), or flung out along rotating magnetic field lines (magnetohydrodynamically, e.g., Blandford & Payne 1982; Proga 2000). While stellar winds may be symmetrical in two dimensions (azimuth and altitude), disk winds are necessarily symmetric in no more than one dimension (azimuth). However, in order to derive some observational constraints on a disk wind hypothesis, we use the same spherically symmetric radiation-driven velocity profile as for the stellar wind but center the wind on the neutron star.

The explicit form of the wind velocity profile is given by:

$$v(R) = v_0 + (v_\infty - v_0)(1 - R_{\text{in}}/R)^\beta \quad (10)$$

where  $v_0$  and  $v_\infty$  are the wind velocities at the stellar surface and at infinity and the parameter  $\beta$  describes the acceleration of the wind. With  $\beta = 0$ , this equation describes a wind which is immediately accelerated to its terminal velocity. The variable  $R$  is the distance from the center of the wind (the center of the companion for the stellar wind or the neutron star for the disk wind). For the stellar wind, the wind begins at the surface of the companion so  $R_{\text{in}} = R_\star$ . For a disk wind however, no such natural inner radius exists and therefore, for the disk wind, we make  $R_{\text{in}}$  an extra parameter of the model and assume that the volume for which  $R < R_{\text{in}}$  is empty. The value of  $R_{\text{in}}$  may correspond, for example, to a characteristic radius on the accretion disk from which the wind arises. Because an accretion disk may be no larger than the Roche lobe of the accreting object, the Roche lobe radius should provide an approximate upper limit on  $R_{\text{in}}$ .

A rearrangement of Equation 7 gives the density distribution.

$$n(R) = \frac{\dot{M}}{4\pi R^2 \mu v(R)}. \quad (11)$$

In order to make use of the scaling relation of Equation 9, we include the velocity profile explicitly (Equation 10) and reexpress the density as follows:

$$n(R) = \left( \frac{\dot{M}}{v_\infty} \right) (4\pi\mu)^{-1} R^{-2} \left[ \frac{v_0}{v_\infty} + \left( 1 - \frac{v_0}{v_\infty} \right) \left( 1 - \frac{R_{\text{in}}}{R} \right)^\beta \right]^{-1}. \quad (12)$$

According to this parameterization, the parameter  $\dot{M}/v_\infty$  plays the role of  $\eta$ . The shape of the DEM distribution is then a function of the parameters  $Lv_\infty/\dot{M}$ ,  $\beta$ ,  $v_0/v_\infty$ , and, for the disk wind,  $R_{\text{in}}$ . For a given choice of those parameters, the magnitude of the DEM distribution is proportional to  $(\dot{M}/v_\infty)^2$  or, equivalently,  $L^2$ .

## 4.2. Calculation of DEM Distributions and Global Spectra

The wind distributions we use are symmetric to rotation around the line containing the neutron star and the center of the companion star. This allowed us to conserve computational resources by using rings around this axis as the spatial cells to calculate the DEM distributions.

The exclusion of the region occulted by the companion star from the apparent DEM breaks this rotational symmetry but we were still able to conserve computation, using rings as the spatial cells, by computing the fraction of each ring not occulted by the companion star and multiplying the emission measure for each ring by that factor. We used the binary system parameters from Table 2, and fixed  $v_0/v_\infty$  at 0.015 which corresponds approximately to the photospheric thermal velocity of an O-type star for  $v_0$  if  $v_\infty$  is of order  $1000 \text{ km s}^{-1}$ . For the spectra which were accumulated during an orbital phase interval longer than 0.02, we averaged the apparent DEM over phases separated by no more than that. Our parameter grid contains the values  $\beta = (0.0, 0.1, 0.2, \dots, 1.5)$ ,  $\log(Lv_\infty/\dot{M}) = (-0.5, -0.33, -0.17, 0, 0.17, \dots, 2.5)$  in units of  $10^{37} \text{ erg s}^{-1}$  for  $L$ ,  $1000 \text{ km s}^{-1}$  for  $v_\infty$  and  $10^{-6} M_\odot \text{ yr}^{-1}$  for  $\dot{M}$ . For the disk wind, the grid also contained  $R_{\text{in}} = (3.16, 5.62, 10, 17.8, 31.6) R_\odot$ . The resultant spectra were stored in a FITS format XSPEC ATABLE file (Arnaud 1995).

In order to demonstrate the appearance and behavior of the DEM distributions, we plot DEM distributions and contour maps of  $\log \xi$  using the best fit parameters found in the following section (§ 4.3, Table 3). In Figure 4 we show a map of  $\log \xi$  for the companion star wind and in Figure 5 we plot the apparent DEM distributions for orbital phases representative of the observed phases. In Figures 6 & 7 we show the same plots for the disk wind model. However, as mentioned in § 4.1, we expect the Roche lobe radius to be an upper limit on  $R_{\text{in}}$  and so we use  $R_{\text{in}} = 3.4 R_\odot$ , the Roche lobe radius as determined from the parameters of Table 2 and the formula of Eggleton (1983), for these plots instead of a best fit value of  $R_{\text{in}}$ . In Figure 7, it can be seen that the apparent emission measure is dramatically reduced during eclipse for a disk wind inner radius significantly smaller than the companion star radius.

### 4.3. Spectral Fitting

For both the disk and the stellar wind models, we simultaneously fit the spectra at all four phases, using for  $f_{\text{plasma}}$  the recombination spectrum for the observable wind at each phase as discussed above. We allowed the parameters of all of the spectral components except for  $f_{\text{plasma}}$  to vary independently for the four observed phases. We show the best fit values and associated errors in Table 3. We show the spectral fits for the stellar wind in Figure 8. The best fit model spectrum for the eclipse phase is shown at high resolution in Figure 9. Since our focus is on the line spectrum, we let the continuum parameters vary to fit the continuum shape without constraining them to physically meaningful bounds. Some strange results were obtained, such as the very large columns, normalizations, and photon indexes for the second power law in the egress phase (for both the stellar and disk wind models). Though the normalizations are very large, the fluxes of this component are comparable to that in the other phases. We note that our best fit value of the neutron star luminosity from the stellar wind model is very near the value obtained by direct measurement of the unocculted continuum. We emphasize that this luminosity value is obtained only from our recombination spectra for wind models, and is determined almost entirely by the

observed line fluxes, not from any direct measurement of the broad band flux.

Both wind models provide acceptable values of  $\chi^2$ , though for the disk wind the fits favor values of the inner radius which are at least comparable to the radius of the companion star. In Figure 10, we plot the value of  $\chi^2$  for the fits as a function of the assumed inner radius. As mentioned in § 4.2, values of  $R_{\text{in}}$  much smaller than the companion star radius lead to dramatic variations in the DEM distribution, and therefore the emission line flux over eclipse. The observed emission line spectrum, however, varies only moderately across the eclipse. As the preferred radii are very large compared to the neutron star Roche-lobe radius, we consider the possibility that the wind could be dominated by matter arising from the accretion disk unlikely.

We compare the lines fluxes predicted by our best fit stellar wind model with line fluxes measured by Ebisawa et al. (1996) in Figure 11. According to our model, the lines from elements with lower values of  $Z$  vary somewhat more as a function of orbital phase. This is because the lines from low- $Z$  ions are produced more efficiently in the region near the surface of the companion star, where the ionization parameter is lower, and which is occulted more during eclipse. Unfortunately, the quality of the current data is not sufficient to test this prediction. Ebisawa et al. (1996) noted that the H-like and He-like lines of iron were undetectable during the first phase (“pre-eclipse”) from which they inferred that the overall ionization parameter was lower at that phase. Our analysis presumes that we observe the same symmetric wind, only occulted differently, at every phase. Therefore, in our model, the line fluxes must be the same at symmetric phases. However, our predicted line fluxes are greater only by a factor of a few from their  $1\sigma$  limits and so our assumption that the wind density distribution and luminosity are constant is not excluded.

## 5. Optical Depth of the Stellar Wind

Until now, we have assumed that the stellar wind is optically thin to X-rays from the neutron star. For the densities and luminosities of our best fit model, the state of X-ray photoionized gas is affected little by optical depth inside an ionized Strömgren-type zone, where the charge state distribution of helium is dominated by  $\text{He}^{++}$  but outside this zone, where the charge state distribution of helium becomes dominated by  $\text{He}^+$ , the effects of optical depth quickly become important (e.g., Kallman & McCray 1982). The size of a Strömgren zone is usually derived for spherically symmetric nebulae (e.g., Osterbrock 1989) with the condition that the rate at which the central source emits photons capable of ionizing helium is equal to the total rate of recombinations which do not produce ionizing photons (i.e., recombinations to excited states). However, the Strömgren radius may also be estimated in a nebula which is not spherically symmetric for any direction from the ionizing source using the condition that the rate of helium ionizing photons emitted per solid angle is equal to the total rate of recombinations per solid angle:

$$\frac{1}{4\pi} \int_{\nu_0}^{\infty} \frac{L_{\nu}}{h\nu} d\nu = \int_0^{R_S} \alpha_B n_e n_{\text{He}^{++}} n_e r^2 dr \quad (13)$$

where  $\alpha_B$  is the recombination rate to excited states and  $\nu_0$  is ionization threshold of  $\text{He}^{++}$  ( $h\nu_0 = 54.4 \text{ eV}$ ). If we assume that the spectrum of Cen X-3 is a power-law with photon index 1, cut off at energies above  $E_{\text{cut}} = 15 \text{ keV}$  (approximately the Santangelo et al. 1998 spectrum) then the integral on the left hand side is

$$LE_{\text{cut}}^{-1} \ln(E_{\text{cut}}/h\nu_0) = \frac{L}{2.67 \text{ keV}} = 2.3 \times 10^{46} \text{ s}^{-1} \quad (14)$$

for  $L = 10^{38} \text{ erg s}^{-1}$ . The computation of the integral on the right-hand side is complicated by the fact that the recombination coefficient,  $\alpha_B$ , is a function of temperature. However, the temperature dependence of  $\alpha_B$  is only  $\sim T^{-1/2}$  and so we can get a good estimate by assuming that the nebula is isothermal. In the calculations of Kallman & McCray (1982), the temperature just inside of the  $\text{He}^{++}/\text{He}^+$  boundary is approximately  $10^5 \text{ K}$  and so we use for  $\alpha_B$  the constant value  $2 \times 10^{-13} \text{ cm}^3 \text{ s}^{-1}$  (Osterbrock 1989, Table 2.8). In the ionized zone, nearly all of the helium is in the form  $\text{He}^{++}$  and so  $n_{\text{He}^{++}} = 8.3 \times 10^{-2} n_e$  almost exactly. The condition that the nebula is optically thin becomes:

$$\int_0^R n_e^2 r^2 dr < 1.1 \times 10^{59} \text{ cm}^{-3}. \quad (15)$$

We note that the quantity on the left hand side is the emission measure per solid angle. For our wind, from the neutron star to the face of the companion along the line of centers, this integral is  $2.72 \times 10^{57} \text{ cm}^{-3}$  and in the direction away from the companion to infinity, it is  $2.98 \times 10^{56} \text{ cm}^{-3}$ . Therefore, it is clear that the assumption that our model wind is optically thin, which we have used to calculate emission spectra, is self-consistent.

## 6. Discussion

We note that our results for the global wind models can be generalized beyond the homogeneous, spherically symmetric distributions we have used. If the wind is clumped on a scale which is small compared to the system such that the ionization parameter inside the clumps and the total emission measure is the same as in a corresponding homogeneous model, then the observed spectrum will be unchanged. To construct such a model where the clumps have a filling factor  $f$ , the density must be increased by a factor  $f^{-1/2}$  to keep  $\int n_e^2 dV$  unchanged and so to keep  $\xi$  unchanged,  $L$  must also be increased by a factor  $f^{-1/2}$ . Because our best fit luminosity is already at the high end of the range of luminosities observed for Cen X-3, the wind cannot be clumped with a filling factor significantly smaller than unity. A similar, though no longer exact, extension can be made to winds that, instead of being confined in small clumps, are confined in solid angle. An example of this scenario is a wind which exists on the surface a cone. Such a geometry is believed to exist in broad absorption line quasars and may be due to preferential launching of the wind along rays from the central object which graze the surface of the accretion disk (e.g., Murray et al. 1995; Proga 2000). For such a geometry, the factor  $\Omega/4\pi$ , where  $\Omega$  is the solid angle to which the wind is confined, plays the same role as  $f$  above. For the same reasons then, we can exclude these types of winds.

Both the stellar wind and the disk wind models give statistically satisfactory fits to the data. However, the best fit values of the inner radius in the disk model are very large compared to the size of the accretion disk. If the extended reprocessing material originates primarily from an accretion disk wind, a geometry in which the wind is prevented from producing recombination radiation inside a radius which is approximately equal to companion star radius (which is  $\sim 4$  times the maximum size of the accretion disk) is required. We believe that it would require fine-tuned conditions to produce such a geometry, and we consider the possibility that a disk wind dominates the extended circumstellar material unlikely.

As we have noted, in our analysis, the mass loss rate and terminal velocity can be obtained only in the combination  $\dot{M}/v_\infty$ . If Doppler shifts of lines due to motion of the wind could be measured, these two parameters could be determined independently. The errors in the line energies quoted by Ebisawa et al. (1996) correspond to velocity upper limits of  $\sim 2000 \text{ km s}^{-1}$  for the iron lines and  $\sim 6000 \text{ km s}^{-1}$  for the lower energy lines. Therefore, only an upper limit on the mass loss rate of the highly ionized wind of  $\sim 3 \times 10^{-6} M_\odot \text{ yr}^{-1}$  can be obtained.

The fact that the value of the luminosity that we obtain from our spectral line fits is very close to the value determined from direct measurements of the continuum gives us confidence that the parameters of our model correspond to unique physical values that accurately describe the stellar wind. For the stellar wind, the best fit values of  $\dot{M}/v_\infty$  and  $\beta$  are similar to those found in isolated stars. For example, for the 06.5 Iaf star HD 163758 and the 06.5 III(f) star HD 190864, the values of  $\dot{M}$  are  $6 \times 10^{-6}$  and  $1.5 \times 10^{-6} M_\odot \text{ yr}^{-1}$  and the values of  $v_\infty$  are 2200 and 2500  $\text{km s}^{-1}$  (Lamers et al. 1999) which corresponds to values of  $\dot{M}/v_\infty$  of  $2.7 \times 10^{-9} M_\odot \text{ yr}^{-1} (\text{km s}^{-1})^{-1}$  and  $0.6 \times 10^{-9} M_\odot \text{ yr}^{-1} (\text{km s}^{-1})^{-1}$  as compared with  $1.56 \pm 0.12 \times 10^{-9} M_\odot \text{ yr}^{-1} (\text{km s}^{-1})^{-1}$  (Table 3) for our fits to the Cen X-3 spectrum. The values of  $\beta$  for these two isolated O stars are 0.7 and 0.8 (Lamers et al. 1999), which are also near our derived value of  $0.57^{+0.06}_{-0.07}$  (Table 3). Therefore, in our model, the best fit wind parameters are roughly consistent with those of the normal radiatively driven winds in isolated massive stars. Considering that the wind is highly ionized and the radiation driving mechanism which governs the structure of the wind in isolated massive stars cannot function, this result is very surprising.

To within an order of magnitude or so, the total emission measure in a smooth wind is given by  $E \sim (\dot{M}/v_\infty)^2 / (m_p^2 R_*)$ . Therefore, to the extent that the companion stars in HMXBs are roughly the same size, lose mass at roughly the same rate, and produce smooth winds with roughly the same terminal velocities, the total emission measures should be approximately equal. Numerically, the above estimate gives, for typical parameters,  $E \sim 10^{59} \text{ cm}^{-3}$ . (Note that this estimate applies equally well to isolated early-type stars.) Clumping in the wind, however, will tend to increase the emission measure. On the other hand, clumping also tends to decrease the local value of  $\xi$ , in effect, removing gas from the high- $\xi$  end of the DEM distribution and adding gas to the lower- $\xi$  end. Thus clumping reduces the wind's X-ray recombination line emission, and increases its fluorescence emission.



We have argued that the Cen X-3 wind is smooth. Sako et al. (1999) have shown that the wind in Vela X-1 is highly clumped. In Figure 12, we compare the DEM distribution derived here for Cen X-3 with that derived, also using X-ray recombination, by Sako et al. (1999) for Vela X-1. The value of  $\dot{M}/v_\infty$  we have derived here for the wind of Cen X-3 is comparable to the value for Vela X-1 derived by a number of methods (Dupree et al. 1980; Sato et al. 1986; Sako et al. 1999). As one caveat, we point out that for Vela X-1 the contribution from fluorescing material, which would cause an upturn in its DEM curve below  $\log \xi \approx 1.5$ , is not included in the plot.<sup>1</sup> Above  $\log \xi = 2.0$ , however, the differences are real, and are quite striking. The relatively small DEM magnitudes in Vela X-1 are a consequence of the fact that most of the mass in the wind is “locked up” in clumps of high density, hence, low  $\xi$ . For example, near  $\log \xi = 3.0$ , where lines from He-like and H-like iron are produced, the DEM magnitudes vary by  $\sim 100$ , which means that these lines are  $\sim 100$  times more luminous in Cen X-3 than in Vela X-1. This does not translate into excessively large line equivalent widths in Cen X-3, however, since its X-ray luminosity is also roughly 100 times higher.

With this comparison arises the question as to what conditions are required in order to produce and/or destroy clumps in X-ray irradiated winds, a subject beyond the scope of this paper, but possibly one that bears on the nature of the wind driving force. The absence of substantial clumping in Cen X-3, as inferred from the modest phase variations of the iron  $K\alpha$  equivalent width, is demonstrated by, and is consistent with, the large DEM magnitudes for  $\log \xi > 2$ . It has been suggested (Sako et al. 1999) that the existence of a clumped wind component in Vela X-1 allows normal radiative driving by the UV field of the companion. Clearly, that is disallowed in the case of Cen X-3. We therefore conclude that the wind is most likely driven by X-ray heating of the illuminated surface of the companion star as proposed by Day & Stevens (1993).

We look forward to *Chandra* observations of this system. High resolution spectroscopic data will allow us to measure independently the lines of the helium-like  $2 \rightarrow 1$  triplets and therefore determine the ionization mechanism directly (Liedahl 1999). We will also be able to measure much smaller velocities (of order  $100 \text{ km s}^{-1}$ ) and therefore be able to set much tighter constraints on the mass-loss rate of the companion and the dynamics of the wind.

## A. Differential Emission Measure

We have defined the emission measure as  $\int n_e^2 dV$ . We now define the ionization parameter limited emission measure as:

$$E(\xi) \equiv \int_{V(\xi' \leq \xi)} n_e^2 dV, \quad (\text{A1})$$

---

<sup>1</sup>Mapping the DEM distribution for low- $\xi$  material based upon X-ray spectra requires much higher spectral resolution, so that fluorescent line complexes can be resolved into their respective charge states.

i.e., the emission measure in the volume in which the ionization parameter is less than some value. The linear differential emission measure is then

$$\frac{dE(\xi)}{d\xi} = \lim_{\delta\xi \rightarrow 0} \frac{E(\xi + \delta\xi) - E(\xi)}{\delta\xi} = \frac{1}{\delta\xi} \int_{V(\xi \leq \xi' \leq \xi + \delta\xi)} n_e^2 dV. \quad (\text{A2})$$

This infinitesimal volume is the space between two surfaces, each of which is defined by a single value of the ionization parameter. The infinitesimal distance between the surfaces is  $\delta\xi/|\nabla\xi|$ . Therefore,

$$\frac{dE(\xi)}{d\xi} = \int_{S(\xi)} \frac{n_e^2}{|\nabla\xi|} dS. \quad (\text{A3})$$

where  $S(\xi)$  and  $dS$  specify the integral over the surface specified by the ionization parameter  $\xi$ . We define the differential emission measure

$$D(\xi) \equiv \frac{dE(\xi)}{d \log \xi} = \int_{S(\xi)} \frac{n_e^2}{|\nabla \log \xi|} dS. \quad (\text{A4})$$

Suppose we have a model for the density distribution such that the density scales linearly with the parameter  $\eta$ . Consider a change of parameters  $\eta \rightarrow \eta'$  and  $L \rightarrow L'$ . The surface defined by  $\xi$  for the unprimed parameters is the same surface defined by

$$\xi' = \frac{L'\eta}{L\eta'} \xi. \quad (\text{A5})$$

Therefore,  $D'(\xi')$  can be related to  $D(\xi)$  by transforming the integrand in Equation A4. Under the parameter change,  $\log \xi$  differs from  $\log \xi'$  by an additive constant and so  $|\nabla \log \xi| = |\nabla \log \xi'|$ . However,  $n_e^2$  is modified by the factor  $(\eta'/\eta)^2$ . Therefore,

$$D'(\xi') = \left( \frac{\eta'}{\eta} \right)^2 D(\xi). \quad (\text{A6})$$

This is Equation 9.

We thank Chris Mauche and Daniel Proga for helpful discussions and careful reading of the manuscript. We also thank John Blondin for helpful discussions. This research has made use of data obtained through the High Energy Astrophysics Science Archive Research Center Online Service, provided by the NASA/Goddard Space Flight Center. This research has made use of NASA's Astrophysics Data System Abstract Service. D. A. L. was supported in part by NASA Long Term Space Astrophysics grant S-92654-F. Work at LLNL was performed under the auspices of the U. S. Department of Energy by University of California Lawrence Livermore National Laboratory under Contract W-7405-Eng-48. M. S. was supported under NASA grant NAG 5-7737.

## REFERENCES

- Alme, M. L. & Wilson, J. R. 1974, *ApJ*, 194, 147
- Anders, E. & Grevesse, N. 1989, *Geochim. Cosmochim. Acta*, 53, 197
- Arnaud, K. A. 1995, The File Format for XSPEC Table Models, Office of Guest Investigator Programs Memo OGIP/92-009, NASA Goddard Space Flight Center Laboratory for High Energy Astrophysics
- Arnaud, K. A. 1996, in *ASP Conf. Series*, Vol. 101, *Astronomical Data Analysis Software and Systems V*, ed. G. Jacoby & J. Barnes, 17
- Arons, J. 1973, *ApJ*, 184, 539
- Ash, T. D. C., Reynolds, A. P., Roche, P., Norton, A. J., Still, M. D., & Morales-Rueda, L. 1999, *MNRAS*, 307, 357
- Audley, M. D. 1998, PhD thesis, Univ. of Maryland
- Basko, M. M. & Sunyaev, R. A. 1973, *Ap&SS*, 23, 117
- Becker, R. H., Pravdo, S. H., Rothschild, R. E., Boldt, E. A., Holt, S. S., Serlemitsos, P. J., & Swank, J. H. 1978, *ApJ*, 221, 912
- Blandford, R. D. & Payne, D. G. 1982, *MNRAS*, 199, 883
- Blondin, J. M. & Woo, J. W. 1995, *ApJ*, 445, 889
- Burderi, L., Di Salvo, T., Robba, N. R., La Barbera, A., & Guainazzi, M. 2000, *ApJ*, 530, 429
- Castor, J. I., Abbott, D. C., & Klein, R. I. 1975, *ApJ*, 195, 157
- Clark, G. W., Minato, J. R., & Mi, G. 1988, *ApJ*, 324, 974
- Conti, P. S. 1978, *A&A*, 63, 225
- Day, C. S. R., Nagase, F., Asai, K., & Takeshima, T. 1993, *ApJ*, 408, 656
- Day, C. S. R. & Stevens, I. R. 1993, *ApJ*, 403, 322
- Dupree, A. K., et al. 1980, *ApJ*, 238, 969
- Ebisawa, K., Day, C. S. R., Kallman, T. R., Nagase, F., Kotani, T., Kawashima, K., Kitamoto, S., & Woo, J. W. 1996, *PASJ*, 48, 425
- Eggleton, P. P. 1983, *ApJ*, 268, 368
- Friend, D. B. & Castor, J. I. 1982, *ApJ*, 261, 293

- Gendreau, K. C. 1995, PhD thesis, Massachusetts Institute of Technology
- Haberl, F., White, N. E., & Kallman, T. R. 1989, *ApJ*, 343, 409
- Hammerschlag-Hensberge, G., Kallman, T. R., & Howarth, I. D. 1984, *ApJ*, 283, 249
- Hatchett, S. & McCray, R. 1977, *ApJ*, 211, 552
- Ho, C. & Arons, J. 1987, *ApJ*, 316, 283
- Hutchings, J. B., Cowley, A. P., Crampton, D., Van Paradus, J., & White, N. E. 1979, *ApJ*, 229, 1079
- Kallman, T. R. & Krolik, J. H. 1999, XSTAR v1.43, HEASARC (NASA/GSFC), Greenbelt, MD
- Kallman, T. R. & McCray, R. 1982, *ApJS*, 50, 263
- Kallman, T. R. & White, N. E. 1982, *ApJ*, 261, L35
- Kawashima, K. & Kitamoto, S. 1996, *PASJ*, 48, L113
- Kitamoto, S., Kawashima, K., Negoro, H., Miyamoto, S., White, N. E., & Nagase, F. 1994, *PASJ*, 46, L105
- Klapisch, M., Schwab, J. L., Fraenkel, J. S., & Oreg, J. 1977, *J. Opt. Soc. Am.*, 61, 148
- Kudritzki, R. P., Pauldrach, A., Puls, J., & Abbott, D. C. 1989, *A&A*, 219, 205
- Lamers, H. J. G. L. M., Haser, S., De Koter, A., & Leitherer, C. 1999, *ApJ*, 516, 872
- Liedahl, D. A. 1999, in *Lecture Notes in Physics*, Vol. 520, *X-Ray Spectroscopy in Astrophysics*, Lectures held at the Tenth Summer School of the European Astrophysics Doctoral Network in Amsterdam, the Netherlands. September 22 - October 3, 1997, ed. J. van Paradijs & J. A. M. Bleeker (New York: Springer-Verlag), 189
- Liedahl, D. A. & Paerels, F. 1996, *ApJ*, 468, L33
- Lucy, L. B. & Solomon, P. M. 1970, *ApJ*, 159, 879
- MacGregor, K. B. & Vitello, P. A. J. 1982, *ApJ*, 259, 267
- Masai, K. 1984, *Ap&SS*, 106, 391
- McCray, R. & Hatchett, S. 1975, *ApJ*, 199, 196
- Mewe, R., Kaastra, J. S., & Liedahl, D. A. 1996, *Legacy*, 6, 16
- Morrison, R. & McCammon, D. 1983, *ApJ*, 270, 119
- Morton, C. D. 1967, *ApJ*, 150, 535

- Murray, N., Chiang, J., Grossman, S. A., & Voit, G. M. 1995, *ApJ*, 451, 498
- Nagase, F., Corbet, R. H. D., Day, C. S. R., Inoue, H., Takeshima, T., Yoshida, K., & Mihara, T. 1992, *ApJ*, 396, 147
- Nagase, F., Hayakawa, S., Sato, N., Masai, K., & Inoue, H. 1986, *PASJ*, 38, 547
- Nagase, F., Zylstra, G., Sonobe, T., Kotani, T., Inoue, H., & Woo, J. 1994, *ApJ*, 436, L1
- Osterbrock, D. E. 1989, "Astrophysics of gaseous nebulae and active galactic nuclei" (Mill Valley, CA: University Science Books)
- Owen, M. P. & Blondin, J. M. 1997, in *American Astronomical Society Meeting*, Vol. 190, 4505
- Proga, D. 2000, *ApJ*, accepted
- Proga, D., Stone, J. M., & Drew, J. E. 1999, *MNRAS*, 310, 476
- Sako, M., Liedahl, D. A., Kahn, S. M., & Paerels, F. 1999, *ApJ*, 525, 921
- Saloman, E. B., Hubble, J. H., & Scofield, J. H. 1988, *At. Data Nucl. Data Tables*, 38
- Santangelo, A., Del Sordo, S., Segreto, A., Dal Fiume, D., Orlandini, M., & Piraino, S. 1998, *A&A*, 340, L55
- Sato, N., Hayakawa, S., Nagase, F., Masai, K., Dotani, T., Inoue, H., Makino, F., Makishima, K., & Ohashi, T. 1986, *PASJ*, 38, 731
- Schreier, E., Levinson, R., Gursky, H., Kellogg, E., Tananbaum, H., & Giacconi, R. 1972, *ApJ*, 172, L79
- Serlemitsos, P. J., Jalota, L., Soong, Y., Kunieda, H., Tawara, Y., Tsusaka, Y., Suzuki, H., Sakima, Y., Yamazaki, T., Yoshioka, H., Furuzawa, A., Yamashita, K., Awaki, H., Itoh, M., Ogasaka, Y., Honda, H., & Uchibori, Y. 1995, *PASJ*, 47, 105
- Stevens, I. R. 1991, *ApJ*, 379, 310
- Tarter, C. B., Tucker, W. H., & Salpeter, E. E. 1969, *ApJ*, 156, 943
- The Ftools Group. 1998, *FTOOLS v4.2*, High Energy Astrophysics Science Archive Reserch Center, NASA Goddard Space Flight Center
- van der Klis, M., Hammerschlag-Hensberge, G., van Paradijs, J. A., Bonnet-Bidaud, J. M., Ilovaisky, S. A., Mouchet, M., Chevalier, C., Glencross, W. M., Willis, A. J., & Zuiderwijk, E. J. 1982, *A&A*, 106, 339
- Vrtilek, S. D., Boroson, B., Cheng, F. H., McCray, R., & Nagase, F. 1997, *ApJ*, 490, 377+
- Wojdowski, P. S., Clark, G. W., & Kallman, T. R. 2000, *ApJ*, in press

- Woo, J. W., Clark, G. W., Blondin, J. M., Kallman, T. R., & Nagase, F. 1995, ApJ, 445, 896
- Woo, J. W., Clark, G. W., Day, C. S. R., Nagase, F., & Takeshima, T. 1994, ApJ, 436, L5
- Woods, D. T., Klein, R. I., Castor, J. I., McKee, C. F., & Bell, J. B. 1996, ApJ, 461, 767

Table 1. Fit Parameters for Eclipse Spectrum

Parameter	Spectral Line Model		
	MEKAL	Variable Abundance MEKAL	Photo
$N_{\text{H1}}$ ( $10^{22} \text{ cm}^{-2}$ )	$0.96^{+0.03}_{-0.02}$	$0.91 \pm 0.02$	$1.03 \pm 0.04$
$E$ ( $10^{58} \text{ cm}^{-3}$ )( $d/10 \text{ kpc}$ ) $^{-2}$	$3.62^{+0.06}_{-0.08}$	$0.17^{+0.09}_{-0.04}$	$2.58^{+0.22}_{-0.27}$
$\log \xi$	...	...	$3.19^{+0.05}_{-0.07}$
$kT$ (keV) <sup>a</sup>	$7.5^{+0.4}_{-0.5}$	$8.9 \pm 0.5$	$0.41 \pm 0.01$
$Z/Z_{\odot}$	1(fixed)	$39^{+112}_{-16}$	1(fixed)
$\alpha_1$	1.5(fixed)	1.5(fixed)	$1.50 \pm 0.09$
$I_{\text{pl1}}$ ( $10^{-3} \text{ s}^{-1} \text{ cm}^{-2} \text{ keV}^{-1}$ )	$< 0.11$	5.6(fixed)	$6.7 \pm 0.6$
$n_{\text{H2}}$ ( $10^{22} \text{ cm}^{-2}$ )	$71^{+10}_{-11}$	$74 \pm 14$	$50^{+11}_{-20}$
$\epsilon_{\text{line}}$ (keV)	$6.41^{+0.018}_{-0.020}$	$6.393^{+0.015}_{-0.017}$	$6.388^{+0.020}_{-0.015}$
$I_{\text{line}}$ ( $10^{-4} \text{ ph cm}^{-2} \text{ s}^{-1}$ )	$3.8^{+0.9}_{-0.8}$	$4.8^{+1.4}_{-0.9}$	$3.3^{+1.2}_{-0.6}$
$\alpha_2$	$1.5 \pm 0.4$	$1.6^{+0.5}_{-0.6}$	$1.5^{+0.7}_{-0.4}$
$I_{\text{pl2}}$ ( $10^{-3} \text{ ph s}^{-1} \text{ cm}^{-2}$ )	$39^{+57}_{-25}$	$11^{+18}_{-7}$	$17^{+79}_{-10}$
$\chi^2/\text{d.o.f.}$	176/170	146/170	176/169
probability <sup>b</sup>	35%	90%	33%

<sup>a</sup>In the case of the photoionized model,  $kT$  is an explicit function of  $\log \xi$ . The error on the temperature is estimated using a local linear approximation to  $T(\log \xi)$ .

<sup>b</sup>Null hypothesis probability

Table 2. Assumed System Parameters for Cen X-3/V779 Cen

Parameter	Value	Reference
$R_{\star}$ (companion radius)	$11.8 R_{\odot}$	a
$a$ (orbital separation)	$19.2 R_{\odot}$	a
$i$ (inclination angle)	$70.2^{\circ}$	a
Distance	10 kpc	b

References. — (a) Ash et al. 1999 (b) Hutchings et al. 1979



Table 3. Global Wind Model Fit Parameters

Parameter	Stellar Wind				Disk Wind			
	Pre-eclipse	Ingress	Eclipse	Egress	Pre-eclipse	Ingress	Eclipse	Egress
$N_{\text{H1}}$ ( $10^{22} \text{ cm}^{-2}$ )	$0.95 \pm 0.08$	$0.97^{+0.02}_{-0.04}$	$1.00^{+0.02}_{-0.04}$	$0.94^{+0.07}_{-0.08}$	$0.86 \pm 0.08$	$0.94^{+0.05}_{-0.04}$	$1.03 \pm 0.04$	$0.87^{+0.07}_{-0.08}$
$\alpha_1$	$0.59^{+0.17}_{-0.15}$	$0.96^{+0.09}_{-0.06}$	$1.42^{+0.11}_{-0.04}$	$-0.18^{+0.07}_{-0.04}$	$0.56^{+0.16}_{-0.14}$	$0.96^{+0.10}_{-0.06}$	$1.41^{+0.12}_{-0.05}$	$-0.19^{+0.03}_{-0.07}$
$I_{\text{p11}}$ ( $10^{-3} \text{ ph cm}^{-2} \text{ s}^{-1} \text{ keV}^{-1}$ )	$17.4^{+3.0}_{-2.4}$	$7.3^{+0.8}_{-0.5}$	$5.8^{+0.7}_{-0.5}$	$3.1^{+0.4}_{-0.3}$	$17.2^{+2.5}_{-2.3}$	$7.3^{+0.9}_{-0.2}$	$5.5^{+0.7}_{-0.2}$	$3.09^{+0.16}_{-0.27}$
$N_{\text{H2}}$ ( $10^{22} \text{ cm}^{-2}$ )	$35^{+8}_{-6}$	$140^{+27}_{-32}$	$50^{+8}_{-14}$	$183^{+35}_{-45}$	$38^{+9}_{-7}$	$154^{+28}_{-36}$	$46^{+15}_{-13}$	$197^{+21}_{-15}$
$\epsilon_{\text{line}}$ (keV)	$6.374^{+0.023}_{-0.027}$	$6.371^{+0.016}_{-0.022}$	$6.391^{+0.017}_{-0.015}$	$6.390 \pm 0.020$	$6.376^{+0.024}_{-0.028}$	$6.371^{+0.017}_{-0.022}$	$6.392^{+0.016}_{-0.015}$	$6.391^{+0.020}_{-0.021}$
$I_{\text{line}}$ ( $10^{-4} \text{ ph cm}^{-2} \text{ s}^{-1}$ )	$23 \pm 5$	$40^{+25}_{-13}$	$3.3^{+0.7}_{-0.6}$	$2.2^{+1.8}_{-0.5} \times 10^2$	$24 \pm 5$	$49^{+18}_{-15}$	$3.2^{+0.8}_{-0.6}$	$27^{+12}_{-6}$
$\alpha_2$	$1.5^{+0.5}_{-0.3}$	$3.3^{+0.6}_{-0.9}$	$1.5^{+0.4}_{-0.5}$	$7.5^{+0.9}_{-0.4}$	$1.6^{+0.5}_{-0.4}$	$3.6^{+0.9}_{-1.0}$	$1.5^{+0.6}_{-0.3}$	$8.0^{+0.1}_{-1.2}$
$I_{\text{p12}}$ ( $10^{-3} \text{ ph cm}^{-2} \text{ s}^{-1} \text{ keV}^{-1}$ )	$2.7^{+4.3}_{-1.3} \times 10^2$	$6.1^{+46}_{-5.4} \times 10^3$	$20^{+35}_{-14}$	$8.3^{+620}_{-0.9} \times 10^7$	$3.3^{+5.8}_{-1.9} \times 10^2$	$1.4^{+6.1}_{-1.3} \times 10^3$	$18^{+39}_{-13}$	$2.6^{+190}_{-1.5} \times 10^8$
$R_{\text{in}}(R_{\odot})$		...				$> 15$		
$\beta$		$0.57^{+0.06}_{-0.07}$				$0.51^{+0.17}_{-0.07}$		
$L v_{\infty} / \dot{M}^{\text{a}}$		$6.8^{+2.0}_{-1.8}$				$15^{+22}_{-6}$		
$\dot{M} / v_{\infty} [d/(10 \text{ kpc})]^{-1}^{\text{a}}$		$1.56 \pm 0.12$				$1.3^{+0.2}_{-0.6}$		
$L [d/(10 \text{ kpc})]^{-1}^{\text{a}}$		$10.7^{+2.9}_{-2.4}$				$20 \pm 9$		
$\chi^2$		552/684				550/683 <sup>b</sup>		

<sup>a</sup>These three expressions are combinations of only two non-degenerate model parameters. The units for these values are such that  $\dot{M}$  has units of  $10^{-6} M_{\odot} \text{ yr}^{-1}$ ,  $v_{\infty}$  units of  $1000 \text{ km s}^{-1}$  and  $L$  units of  $10^{37} \text{ erg s}^{-1}$ .

<sup>b</sup>for  $R_{\text{in}} = 30 R_{\odot}$

Table 4. Stellar Wind Model  $n = 2 \rightarrow 1$  Line Fluxes<sup>a</sup>

Line		Phase Range			
Ion	Energy(keV) <sup>b</sup>	-0.31 – -0.29	-0.23 – -0.08	-0.08 – 0.13	0.14 – 0.20
Ne X	1.022	4.7	2.7	1.9	3.0
Mg XII	1.472	1.7	1.0	0.7	1.0
Si XIV	2.006	2.0	1.3	1.0	1.4
S XVI	2.621	1.7	1.2	0.9	1.2
Fe XXV	6.667	4.9	3.6	3.2	3.6
Fe XXVI	6.966	2.8	2.2	2.0	2.3

<sup>a</sup>In units of  $10^{-4} \text{ ph cm}^{-2} \text{ s}^{-1}$  are summed over line complexes and energies are for centroids of complexes.

<sup>b</sup>For He-like ions, the centroid energy of the line complex.

Fig. 1.— The fit to the eclipse spectrum using the MEKAL collisionally ionized plasma model. The crosses represent the data. The solid line represents the total model spectrum and the dashed and dotted lines represent the components of the model spectrum. The MEKAL model (lines and bremsstrahlung continuum) accounts for nearly all of the observed flux below  $\sim 5$  keV. Power law 2 and the 6.4 keV line make up the remainder of the flux at high energy. No room for a Compton scattered continuum remains below 5 keV.

Fig. 2.— The eclipse spectrum fit with the MEKAL model with variable abundance. Here, the power law is larger than the MEKAL component at low energies though the emission features are approximately the same as in solar abundance fit.

Fig. 3.— The fit using the single-zone recombination model. The recombination line and RRC spectrum (second largest component in 1–2 keV region) is plotted as a component separate from the 0.4 keV bremsstrahlung (small component peaking near 1.3 keV). In PIE, the observed lines are produced at a much cooler temperature than in CIE. Therefore, in PIE the bremsstrahlung continuum is much weaker and there is room for a Compton scattered continuum (which is represented by the two large continuum components).

Fig. 4.— Contour plot of ionization parameter distribution for the stellar wind in the orbital plane. Contours of constant  $\log \xi$  are indicated. Dashed lines delineate the region which is not visible when the system is viewed from an orientation opposite the neutron star. The position of the neutron star is indicated by crosshairs.

Fig. 5.— Apparent DEM distributions for the best fit stellar wind model parameters as viewed at three phases characteristic of the *ASCA* observation. At eclipse center (phase 0) the regions of highest  $\xi$  (near the neutron star) and the regions of lowest ionization parameter (near the stellar surface) are highly occulted. Away from eclipse center the DEM increases at all values of  $\xi$  as more of the wind becomes visible, though the increase is most dramatic at the highest and lowest values of  $\xi$ .

Fig. 6.— Contour plot of ionization parameter distribution for a disk wind with parameters of Table 3 except with  $R_{\text{in}} = 3.4R_{\odot}$ , the Roche-lobe radius. In this model, the region inside the innermost contour has zero density. At large radii, the density varies as  $R^{-2}$  and so  $\xi$  approaches a constant value.

Fig. 7.— The apparent differential emission measure for the disk wind for orbital phases characteristic of this observation. The model parameters are the same as in Figure 6. Most of the emission measure comes from radii not much larger than  $R_{\text{in}}$ . Therefore, if  $R_{\text{in}}$  is much smaller than the companion star, most of the emission measure, and all of the emission measure at lower values of  $\xi$  is occulted during eclipse. The apparent emission measure in eclipse is about one-tenth that outside of eclipse here.

Fig. 8.— The best fit to the *ASCA* spectra with the stellar wind model. The crosses represent the

data. The dashed and dotted lines represent the two absorbed power-law continuum components, the Fe  $K\alpha$  line, and the recombination component and the solid line represents the total model spectrum.

Fig. 9.— The eclipse phase model spectrum. The solid line indicates the total flux and the broken lines indicate the fluxes of the absorbed power-law continua. Among the features not labeled are several Fe  $3\rightarrow 2$  lines in the 1–2 keV range. Between Si XIV  $Ly\beta$  at 2.375 keV and S XVI  $Ly\alpha$  at 2.621 keV is the S XV  $2\rightarrow 1$  complex and higher order Lyman lines of Si XIV.

Fig. 10.—  $\chi^2$  vs. inner wind radius for the disk wind model. The horizontal lines indicate confidence intervals. The vertical line represent the neutron star Roche lobe radius, the distance from the neutron star to the stellar surface.

Fig. 11.— Our best fit stellar wind model line fluxes ( $\circ$ ) and Ebisawa et al. (1996) measured line fluxes ( $\times$ ). Our model line fluxes are always within three sigma of the fit values. All fluxes have been corrected for interstellar absorption ( $N_{H1}$ ).

Fig. 12.— A comparison of the DEM distributions for Cen X-3 and Vela X-1.

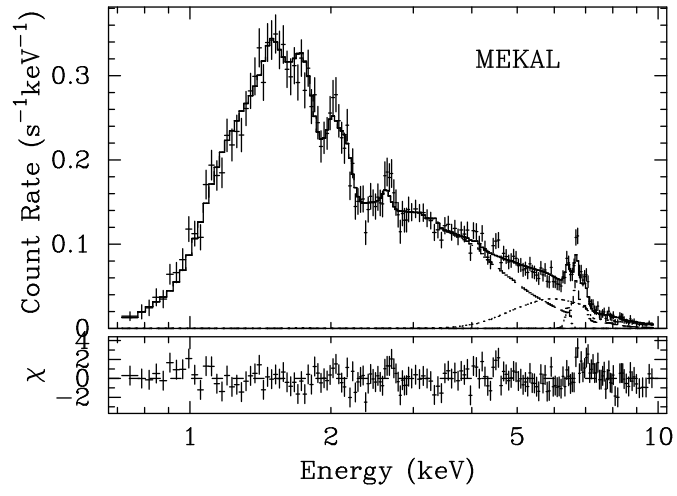


Figure 1

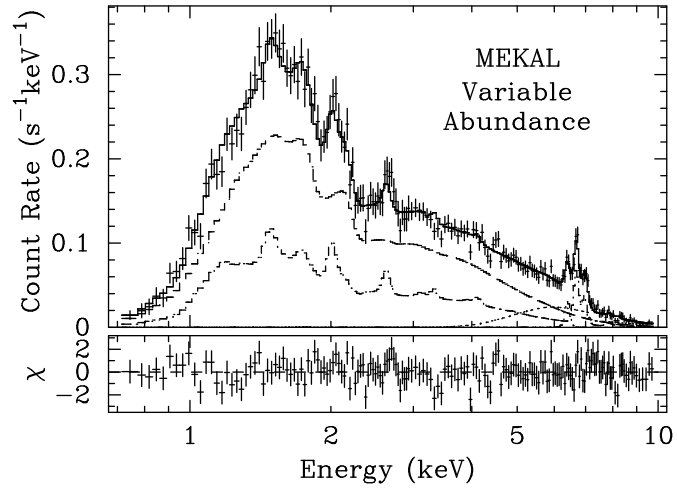


Figure 2

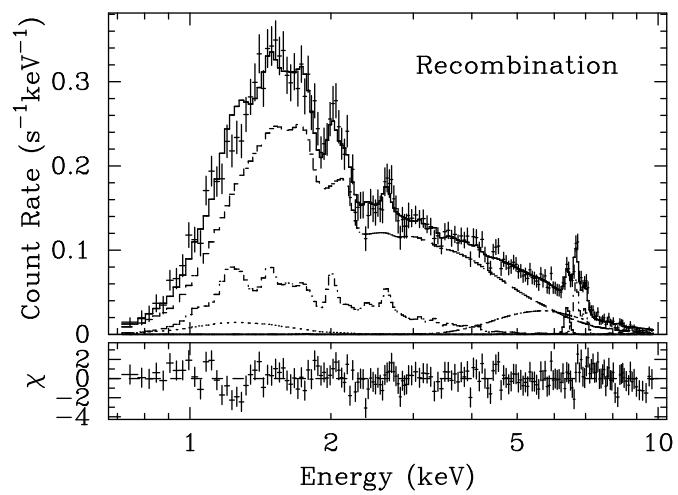


Figure 3

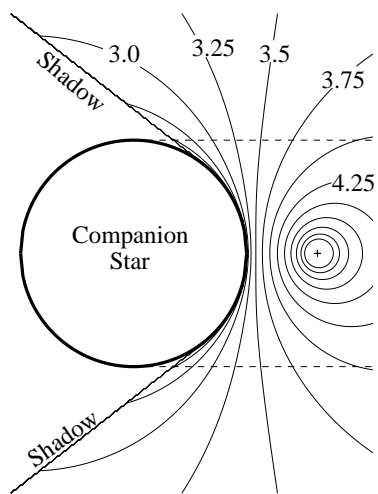


Figure 4

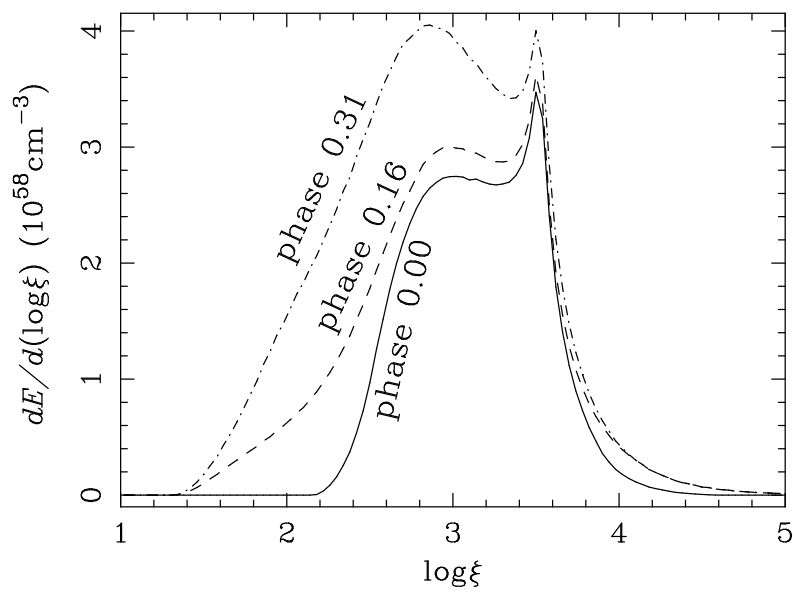


Figure 5

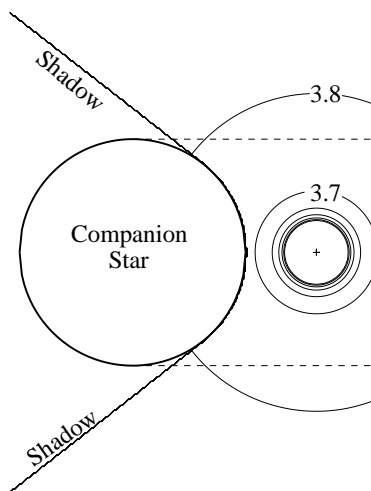


Figure 6

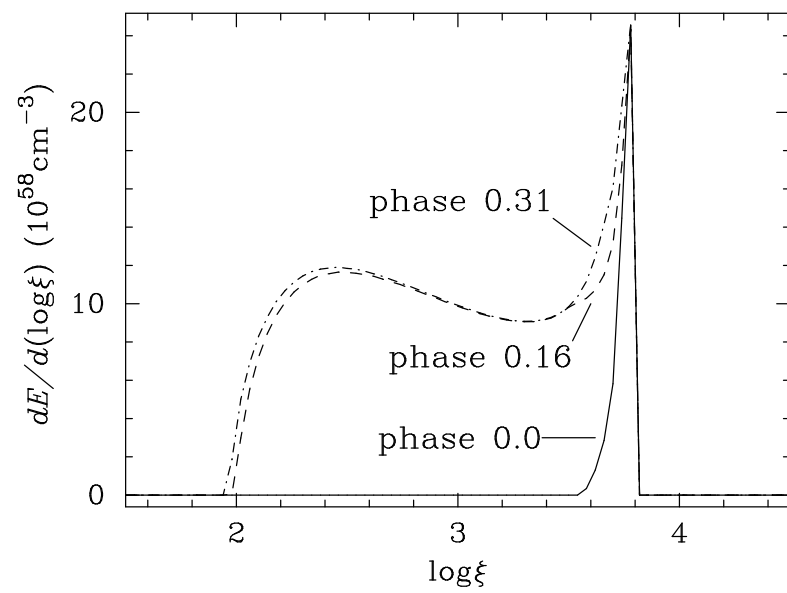


Figure 7



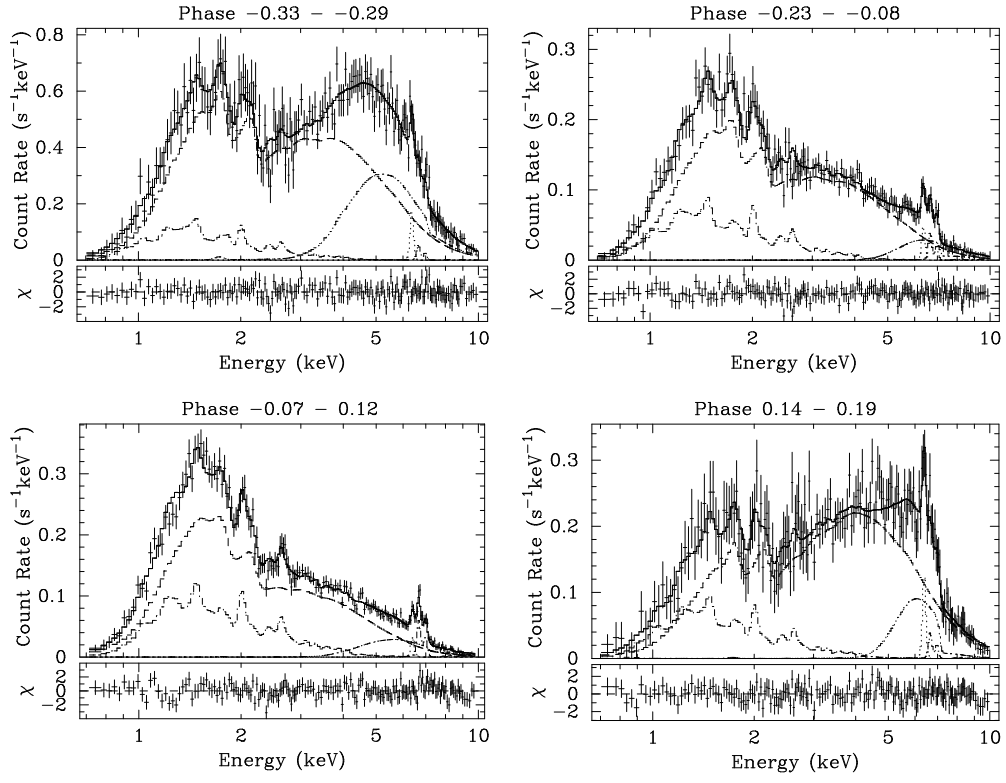


Figure 8a,b,c,d

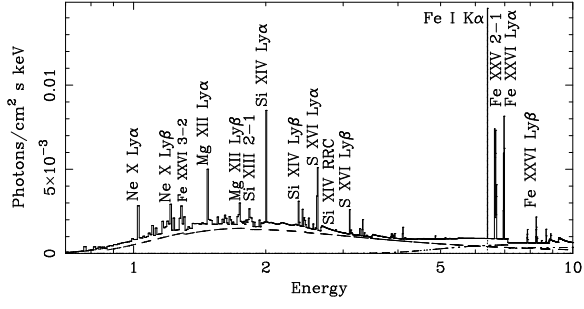


Figure 9

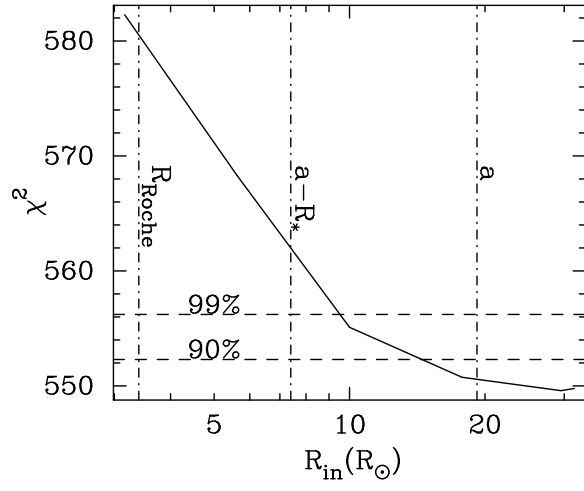


Figure 10

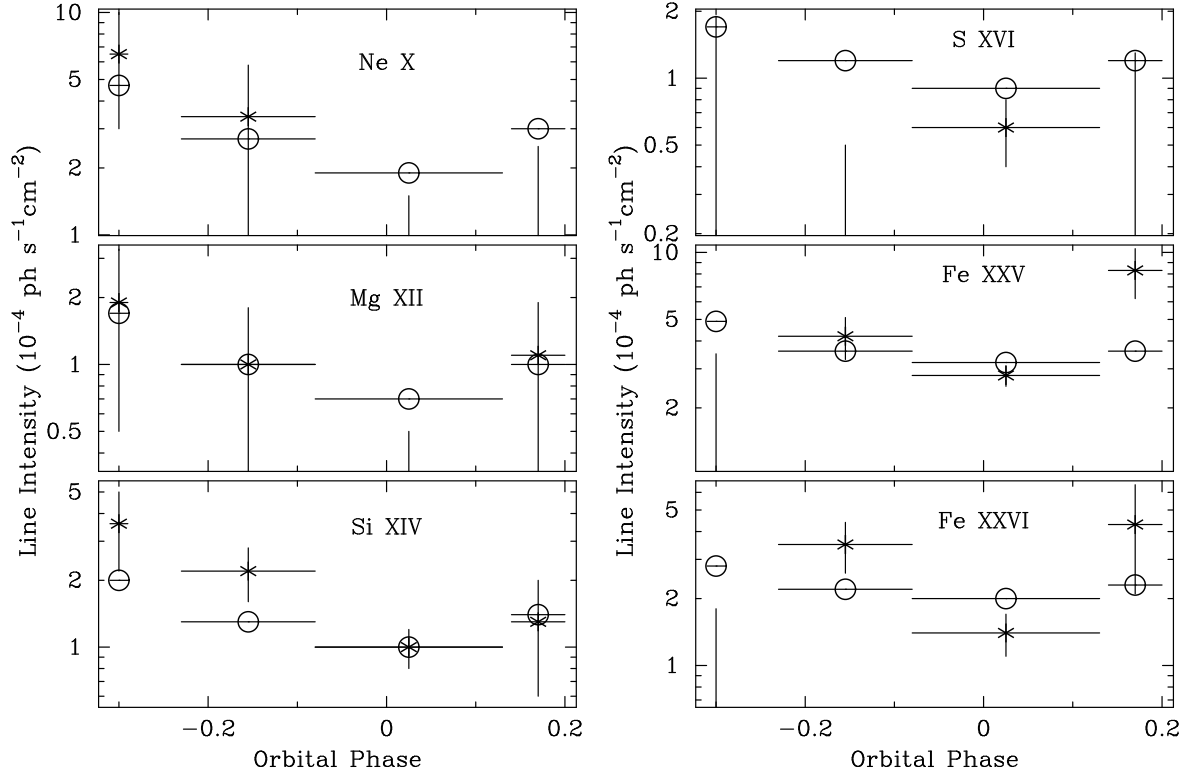


Figure 11

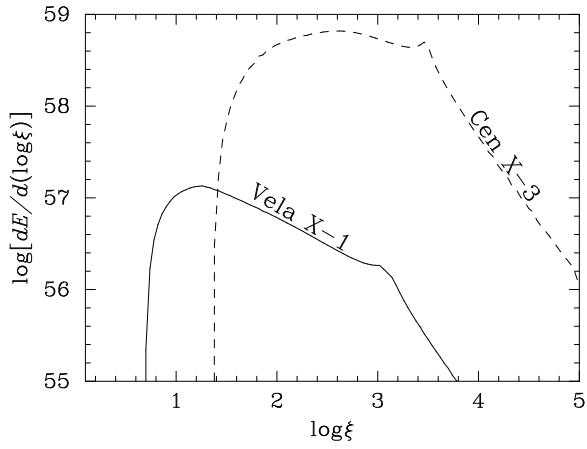


Figure 12